

Article

Three-Dimensional Hole Size (3DHS) Approach for Water Flow Turbulence Analysis over Emerging Sand Bars: Flume-Scale Experiments

Mohammad Amir Khan ¹, Nayan Sharma ², Giuseppe Francesco Cesare Lama ^{3,*}, Murtaza Hasan ⁴, Rishav Garg ¹, Gianluigi Busico ⁵ and Raied Saad Alharbi ⁶

¹ Department of Civil Engineering, Galgotia College of Engineering, Knowledge Park I, Greater Noida 201310, India; amirdamu@gmail.com (M.A.K.); rishavgarg@science.in (R.G.)

² Center for Environmental Sciences & Engineering (CESE), Shiv Nadar University, Uttar Pradesh 201314, India; nayanfwt1@gmail.com

³ Department of Civil, Architectural and Environmental Engineering (DICEA), University of Naples, Federico II, 80125 Napoli, Italy

⁴ Department of Civil Engineering, Chandigarh University, Mohali 140413, India; murtazadce@gmail.com

⁵ Department of Environmental, Biological and Pharmaceutical Sciences and Technologies, Campania University Luigi Vanvitelli, 81100 Caserta, Italy; gianluigi.busico@unicampania.it

⁶ Department of Civil Engineering, College of Engineering, King Saud University, P.O. Box 800, Riyadh 11421, Saudi Arabia; rsalharbi@ksu.edu.sa

* Correspondence: giuseppecesare.lama@unina.it; Tel.: +39-081-253-9423



Citation: Khan, M.A.; Sharma, N.; Lama, G.F.C.; Hasan, M.; Garg, R.; Busico, G.; Alharbi, R.S.

Three-Dimensional Hole Size (3DHS) Approach for Water Flow Turbulence Analysis over Emerging Sand Bars: Flume-Scale Experiments. *Water* **2022**, *14*, 1889. <https://doi.org/10.3390/w14121889>

Academic Editor: Bommanna Krishnappan

Received: 22 May 2022

Accepted: 10 June 2022

Published: 12 June 2022

Publisher's Note: MDPI stays neutral with regard to jurisdictional claims in published maps and institutional affiliations.



Copyright: © 2022 by the authors. Licensee MDPI, Basel, Switzerland. This article is an open access article distributed under the terms and conditions of the Creative Commons Attribution (CC BY) license (<https://creativecommons.org/licenses/by/4.0/>).

Abstract: The many hydrodynamic implications associated with the geomorphological evolution of braided rivers are still not profoundly examined in both experimental and numerical analyses, due to the generation of three-dimensional turbulence structures around sediment bars. In this experimental research, the 3D velocity fields were measured through an acoustic Doppler velocimeter during flume-scale laboratory experimental runs over an emerging sand bar model, to reproduce the hydrodynamic conditions of real braided rivers, and the 3D Turbulent Kinetic Energy (TKE) components were analyzed and discussed here in detail. Given the three-dimensionality of the examined water flow in the proximity of the experimental bar, the statistical analysis of the octagonal bursting events was applied to analyze and discuss the different flume-scale 3D turbulence structures. The main novelty of this study is the proposal of the 3D Hole Size (3DHS) analysis, used for separating the extreme events observed in the experimental runs from the low-intensity events.

Keywords: flume-scale analysis; ADV; flow-bar interaction; 3D turbulence; TKE; octagonal bursting events; 3DHS

1. Introduction

Alluvial rivers characterized by high fluvial energy are typically affected by braiding phenomena, and the emergence of sediment bars is considered the prominent origin of complex morphologies associated with their formation [1,2]. The morphological variations occurring in braided streams are closely related to bank erosion, as a direct consequence of water flow—sediment transport interplay over time [3–6].

In this framework, the proper analysis of the main turbulence traits induced by the presence of bars within braided rivers is crucial from both morphological and hydrodynamic perspectives [7–12]. Among others, McSherry et al. [13] and Jalalabadi et al. [14] have observed that bursting turbulent events can be effectively coupled to the classical threshold shear stress theory for the prediction of particles entrainment mechanisms [15–17]. In recent hydro-geomorphological numerical and experimental research, the study of the coherent structures corresponding to emerging bars was analyzed for correlating sediment transport to instantaneous bursting events [18–23]. In hydrodynamics, the study of the 2D

turbulent flow structures in the vicinity of the wall is generally performed by applying the well-known quadrant events analysis [24,25], whilst it is not sufficiently rigorous and satisfactory when analyzing 3D water flows [26–29]. In these cases, Leary and Schmeeckle [30] and Schobesberger et al. [31] have recently applied the so-called analysis of the octagonal bursting events [32–34], also known as octant events analysis, for overpassing the classical Reynolds stress approach [35,36].

The goal of the present experimental study is the analysis of the flume-scale 3D turbulence traits observable in the proximity of an emerging bar model. The 3D Turbulent Kinetic Energy (hereinafter indicated as TKE) components were evaluated here, and the whole flow turbulence was then examined by analyzing the octagonal bursting events approach. Following the study of Guan et al. [37] among others, the so-defined 3D Hole Size (3DHS) method was proposed in this study for segregating the extreme events from the low-intensity ones at the proximity of the examined emerging sand bar for the first time in the analysis of the turbulence traits observed during flume-scale laboratory experiments.

2. Materials and Methods

2.1. Laboratory Experiments

As shown in Figure 1, the experimental runs were carried out in a 3 m wide, 1 m deep, and 12 m long concrete flume located in the River Engineering Laboratory of the Department of Water Resources Development and Management at the Roorkee Indian Institute of Technology (India), under constant bed slope and discharge values of 0.005 and $0.25 \text{ m}^3 \text{ s}^{-1}$, respectively. The x direction corresponds to the water flow direction.

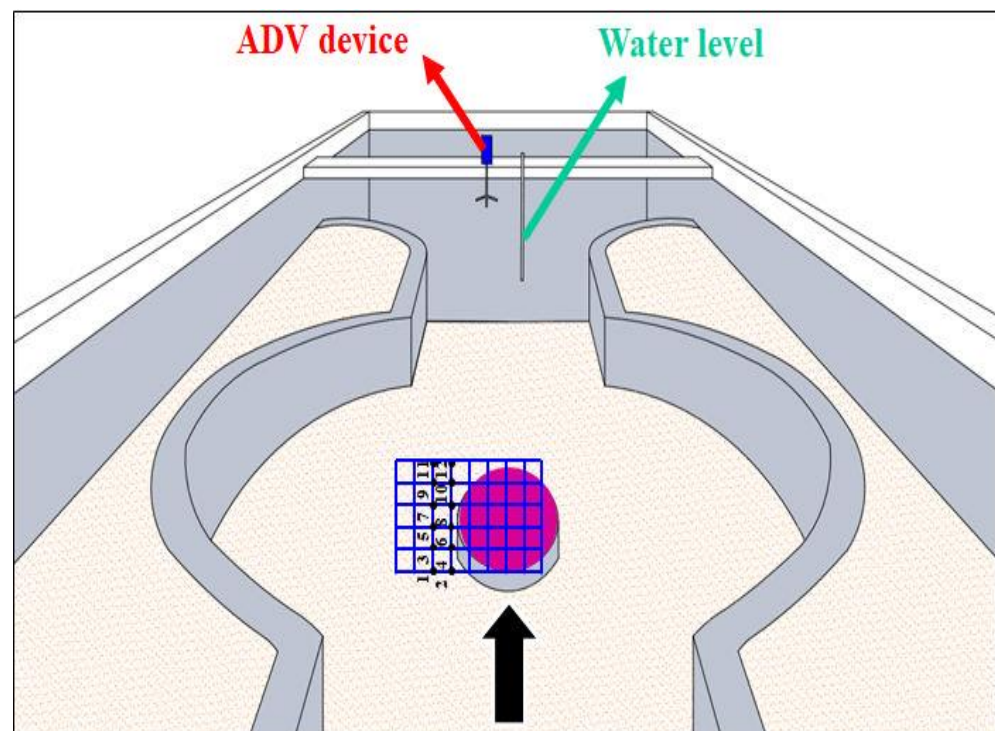


Figure 1. Overview of the laboratory flume employed in the present experimental study, with detailed views of the ADV device, the emerging bar (purple ellipse), and the measuring grid (in blue) composed of $10 \text{ cm} \times 10 \text{ cm}$ cells. The black arrow denotes the flow direction. The measuring points analyzed are indicated listed from 1 to 12.

In the present experimental study, the 3D velocity components over x, y, and z directions in the proximity of the examined emerging sand bar [38–43], respectively indicated as streamwise (u), spanwise (v), and vertical (w) velocity components, were measured by using a 4-beam down-looking acoustic Doppler velocimeter (ADV) device [44–48] with an

acquisition frequency of 20 Hz. The time-series data having a signal average Correlation coefficient—the average correlation between acoustic wave signals recorded by each couple of ADV beams—of less than 0.70 were excluded from the further data processing [49–52]. Due to the massive presence of sediment particles during the runs, all the experiments were carried out in clear water conditions. The shear stress in the flume is kept below the critical shear stress.

The results of the error analysis of ADV measurements are shown in Table 1.

Table 1. Values of errors ADV measurements (in mm s^{-1}).

Flow Velocity Range (mm s^{-1})	ADV Error Range (mm s^{-1})
± 50	± 0.88
± 100	± 0.83
± 200	± 1.01

The results of the previous analysis indicate that the velocity errors in ADV measurement lie in the typical range of flume-scale experimental analysis, as highlighted by Nikou et al. [51].

Aiming at reducing as much as possible the well-known fluid dynamic end-wall effects on the turbulent water flow behaviour in the proximity of the examined emerging sand bar [50,51], the concrete flume's width was increased in the central region, as shown in Figure 1.

The bed of the experimental concrete flume was composed of uniform grading sand, having a value of d_{50} equal to 0.25 mm, with d_{50} indicating the so-called mass-median-diameter of the sediments' particle size distribution, as shown by many previous studies of ecohydraulic, environmental, and river engineering interest [53–61]. At each experimental run, the 3D velocity components were measured at 24 different points belonging to a measuring grid composed of $10 \text{ cm} \times 10 \text{ cm}$ cells, and only 12 measuring points were selected for the further experimental analyses, named from “1” to “12”.

In more detail, the experimental emerging sand bar was kept at a constant depth of 32 cm for all runs, while the submergence ratio, defined as the ratio of the bar height to the water level, was different at each run. The bed elevation measurements were computed aiming at assuring that positive values indicate the depositional region while negative values indicate the scouring. In the present study case, the only experimental run 1R was performed with no emerging bar in the flume.

The experimental flume-scale conditions adopted in the present flume-scale study are indicated in Table 2.

Table 2. Details of the experimental runs performed in this study: l (cm), b (cm), and h_b (cm) are the major and the minor dimension, and the height from the flume bed of the emerging sand bar model, respectively, while h_b/h is the submergence ratio.

Experimental Run	h_b/h	$b \times l \times h_b$
1R	-	-
2R	0.25	$80 \times 130 \times 8$
3R	0.31	$80 \times 130 \times 10$
4R	0.41	$80 \times 130 \times 13$
5R	0.47	$80 \times 130 \times 15$
6R	0.53	$80 \times 130 \times 17$
7R	0.59	$80 \times 130 \times 19$
8R	0.66	$80 \times 130 \times 21$
9R	0.72	$80 \times 130 \times 23$
10R	0.81	$80 \times 130 \times 26$
11R	0.88	$80 \times 130 \times 28$
12R	0.90	$80 \times 130 \times 29$

Since the hydrodynamic effect of turbulence bursting events is prevailing close to the experimental flume bed [62–64], the 3D velocity components were measured at the near-bed flume region, along 15 relative depths z/h , where z is the elevation of each measuring point on the emerging sand bar from the flume bed and h is the measured water level: 0.031, 0.038, 0.047, 0.056, 0.063, 0.069, 0.071, 0.073, 0.075, 0.078, 0.081, 0.083, 0.087, 0.093, and 0.097.

2.2. Experimental TKE Analysis

In the present experimental study case, the so-defined total TKE was computed by applying the following equation [65]:

$$\text{TKE} = \frac{1}{2} \left(\overline{u'^2} + \overline{v'^2} + \overline{w'^2} \right), \quad (1)$$

where u' , v' , and w' are the so-called 3D velocity fluctuation components over x , y , and z axes, respectively.

The three-dimensional TKE components in x , y , and z directions were then obtained as follows:

$$\text{TKE}_x = \frac{1}{2} \overline{u'^2}, \quad (2)$$

$$\text{TKE}_y = \frac{1}{2} \overline{v'^2}, \quad (3)$$

and

$$\text{TKE}_z = \frac{1}{2} \overline{w'^2}. \quad (4)$$

In Equations (1)–(4) the horizontal top bars indicate Reynolds-type time-average values of the 3D velocity fluctuation components.

2.3. Analysis of Octagonal Bursting Events

In the present experimental study, the 3D flow structures induced by the experimental emerging sand bar were analyzed by applying the so-called octagonal bursting events approach [66], based on the sign of the experimental three-dimensional velocity fluctuations components [67–69].

The occurrence probabilities associated with each octagonal bursting event $P_\zeta = n_\zeta/N$ in the single octant ζ , where n_ζ is the total amount of bursting events associated with each octant ζ , and N represents the total extension of the single examined ADV signal for all octants [70–75].

The detailed schematic overview of the eight classes of occurrence probabilities associated with the octagonal turbulence bursting events, namely from P_1 to P_8 , is shown in the following Figure 2.

2.4. Analysis of Three-Dimensional Hole Size (3DHS)

As remarked by Di Bernardino [76] among others, low-intensity octagonal turbulence bursting events do not furnish any contribution to the turbulent burst, then it is possible applying the concept of Hole size analysis, used in fluid dynamics for the experimental analysis of 2D bursting events [77–79], in regions where the water flow is highly three-dimensional. In these cases, the combination of the Hole Size approach with octagonal turbulence bursting events analysis is extremely useful for distinguishing the extreme octagonal events from the low-intensity ones. Therefore, the three-dimensional Hole Size (3DHS) analysis is a novel threshold method proposed in the present experimental study for stretching the capabilities of the 2D Hole size analysis to the study of the 3D octagonal turbulence bursting events [80,81].

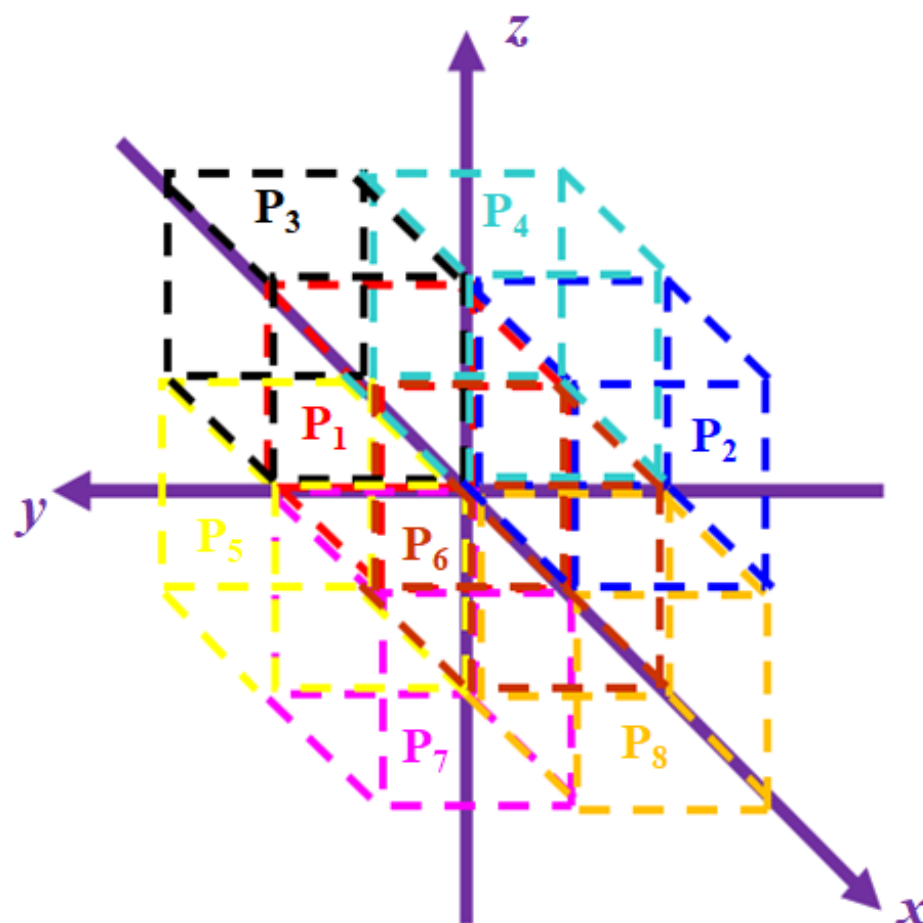


Figure 2. Schematic overview of the occurrence probability (from P_1 to P_8) associated with the octants ζ .

In analogy with the 2D Hole size [82–87], the 3DHS analysis was employed here for extracting from all the ADV time-series velocity signals the 3D turbulent velocity values higher than H times the product of the root mean square of the three velocity fluctuation components: $|u' v' w'| > H \bar{u} \bar{v} \bar{w}$.

3. Results and Discussion

3.1. Experimental TKE Analysis

The depth-averaged contour maps of TKE components over x , y , and z directions are shown in detail in Figures 3–7 for the experimental runs 1R, 2R, 4R, 6R, and 10R, respectively. In all Figures, L is the total length of the reference grid in the x direction, while the origin of the x and y axes is located at the bar bottom, at its center.

It emerges from the observation of Figure 3a–c that, for 1R run, no defined turbulence pattern can be recognized, and extremely low TKE values over x , y , and z directions were observed. This is due to the absence of the emerging sand bar. In more detail, TKE_x and TKE_y contour maps showed very poor fixed patterns, with decreasing values at growing transverse distances y/L . As indicated in Figure 4a–c, high-value TKE_x and TKE_y contours were retrieved near the upstream end of the examined emerging sand bar at the experimental run 2R, with a decreasing behavior towards its downstream end, while TKE_z contours do not furnish any fixed turbulence structure. Also, it was possible observing from the direct comparison of Figures 5–7 that the values of the TKE components in the three directions increase with h_b/h , indicating that the augmentation in the height of the examined emerging sand bar induced high turbulence production trends.

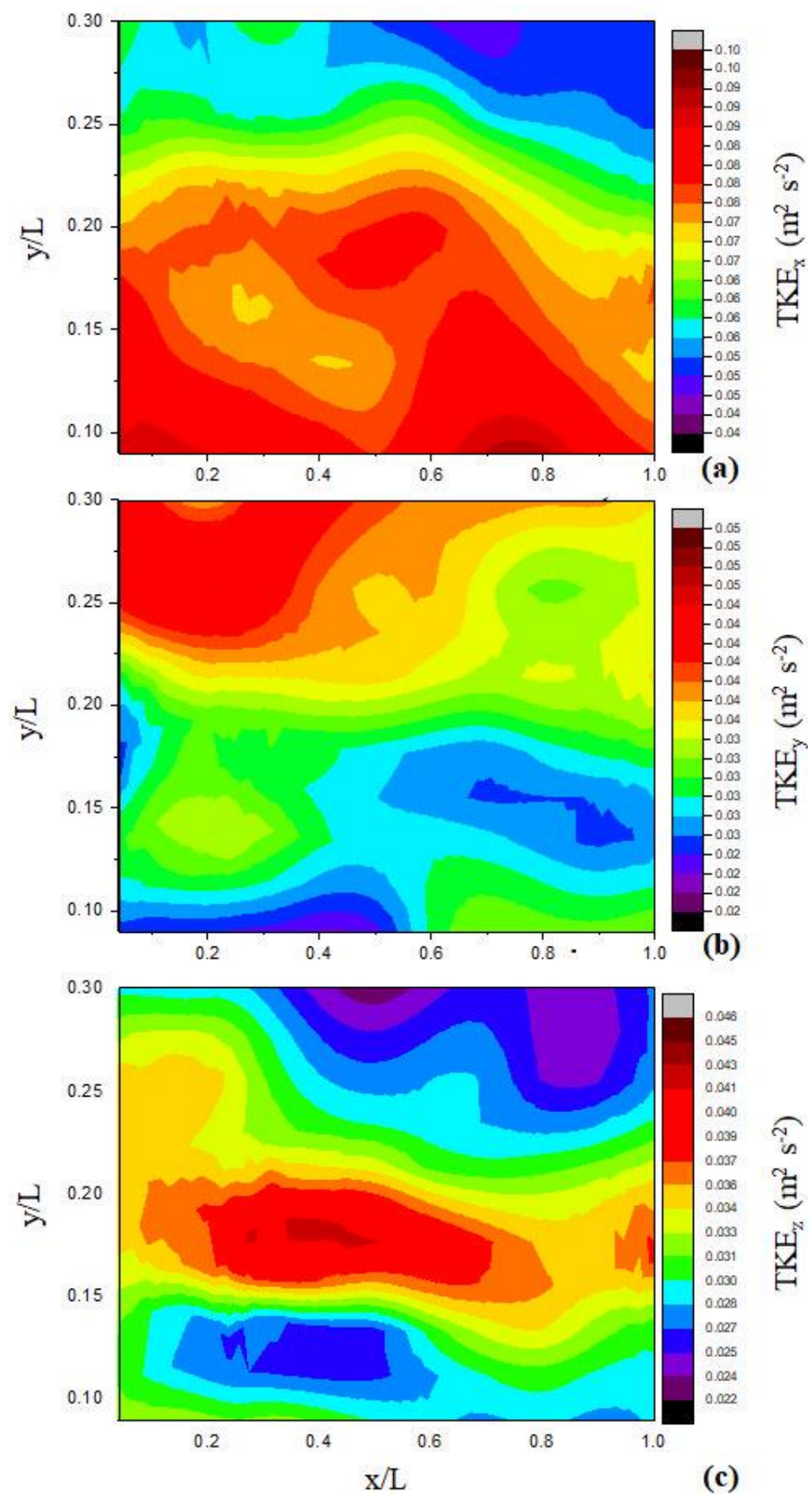


Figure 3. Contour maps of depth-averaged (a) TKE_x , (b) TKE_y , and (c) TKE_z for the experimental run 1R (no sand bar emerging from the flume bed).

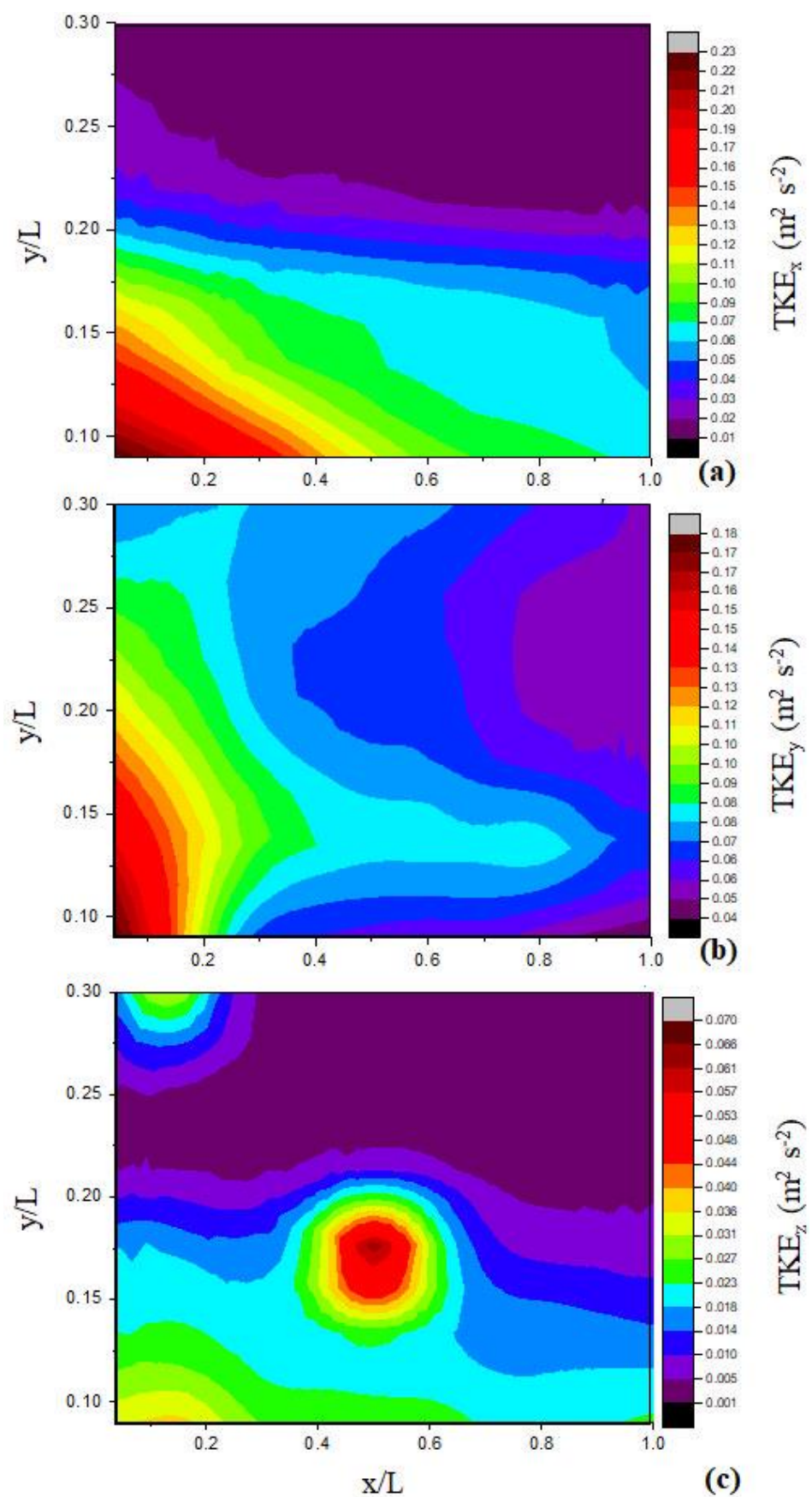


Figure 4. Contour maps of depth-averaged (a) TKE_x , (b) TKE_y , and (c) TKE_z for the experimental run 2R.

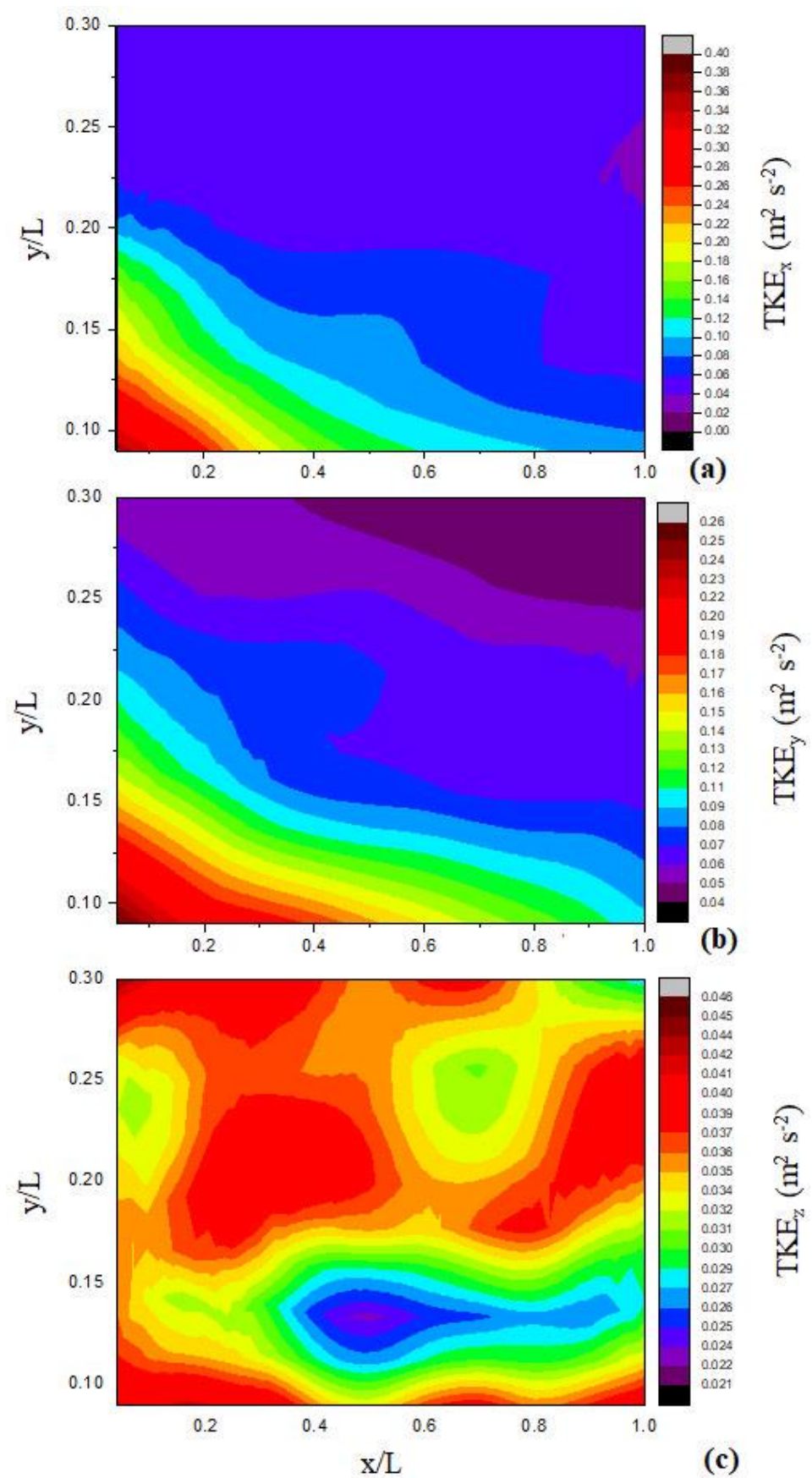


Figure 5. Contour maps of depth-averaged (a) TKE_x , (b) TKE_y , and (c) TKE_z for the experimental run 4R.

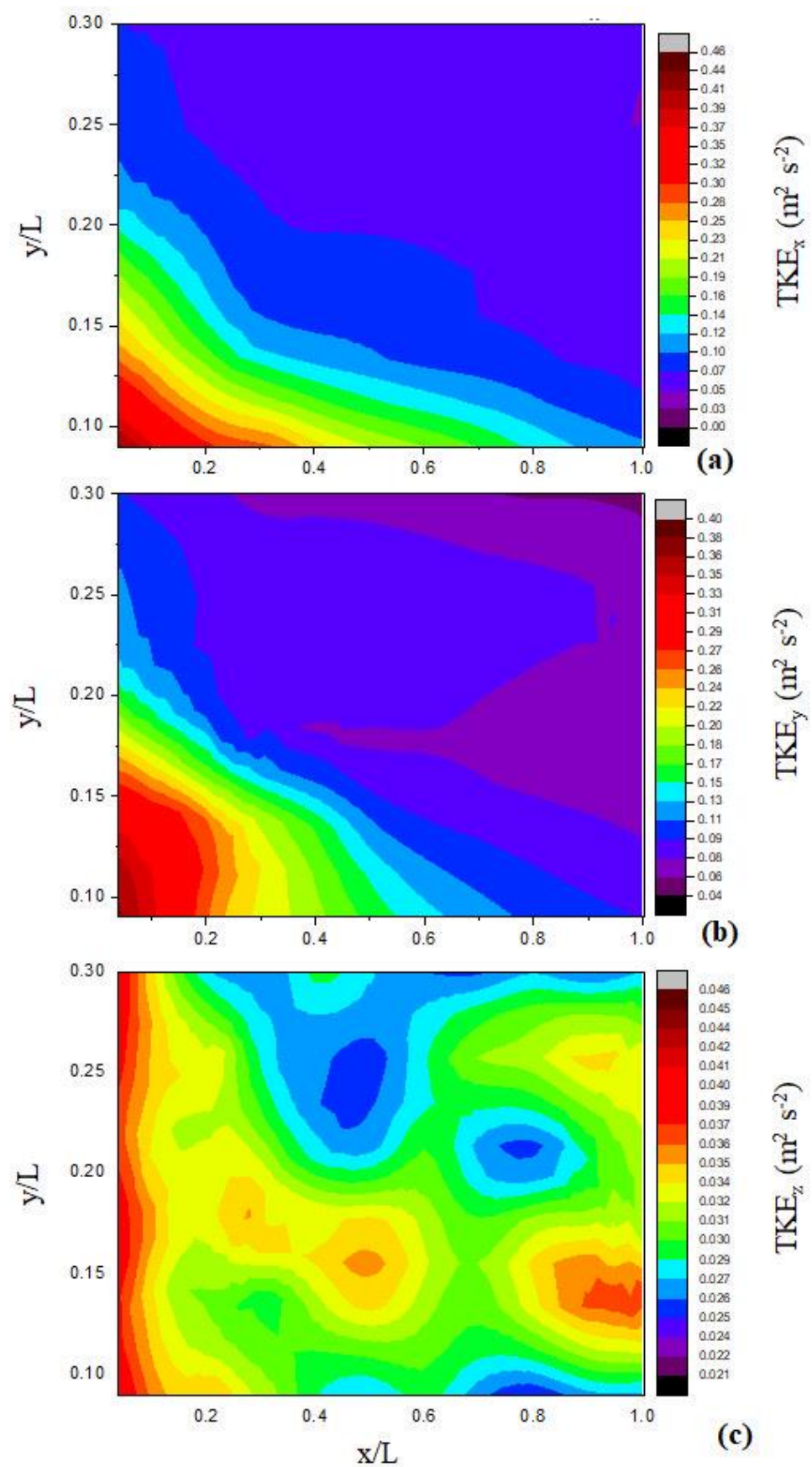


Figure 6. Contour maps of depth-averaged (a) TKE_x , (b) TKE_y , and (c) TKE_z for the experimental run 6R.

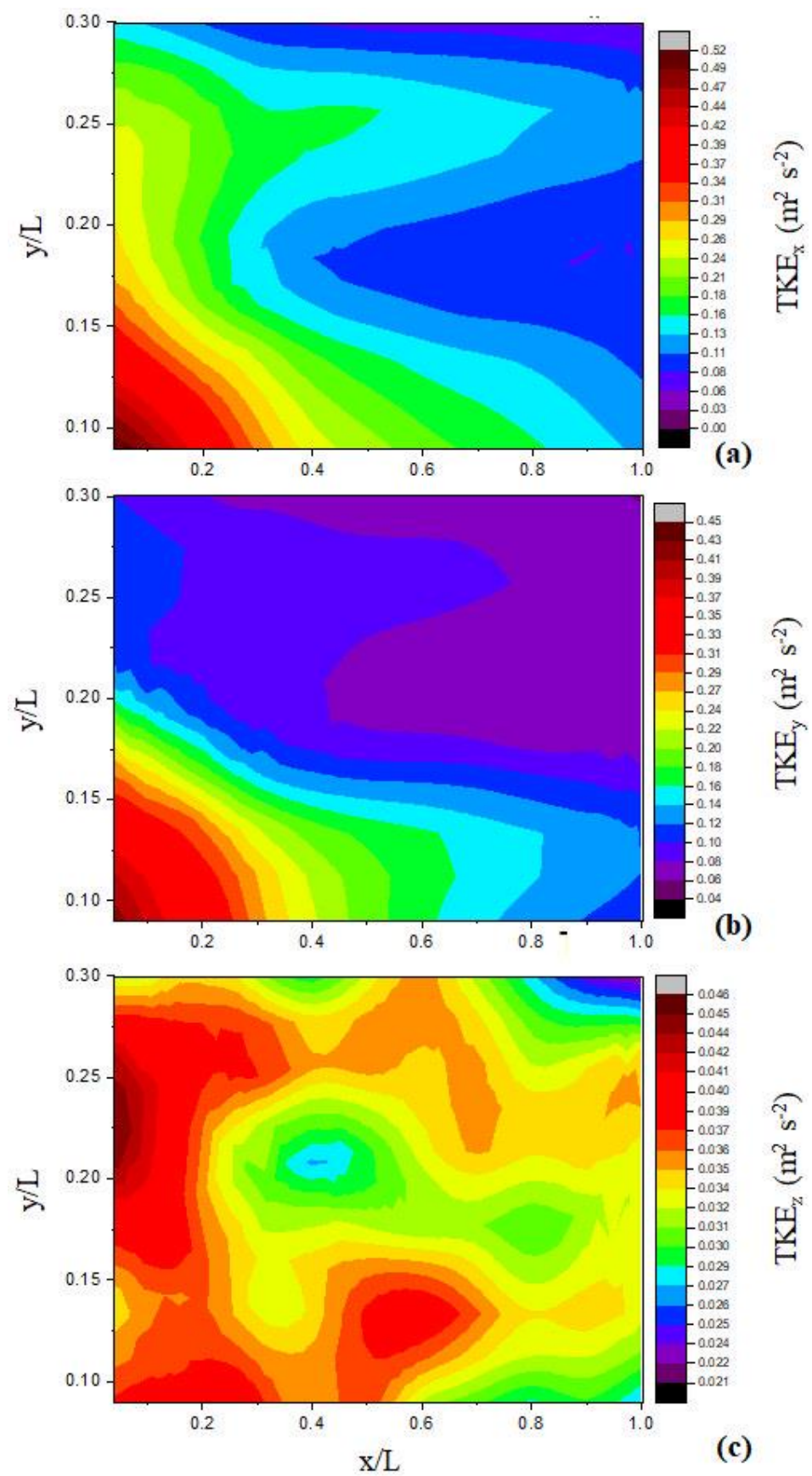


Figure 7. Contour maps of depth-averaged (a) TKE_x , (b) TKE_y , and (c) TKE_z for the experimental run 10R.

3.2. Analysis of Octagonal Bursting Events

The following Figures 8–11 illustrate the contour maps of depth-averaged occurrence probabilities associated with each octagonal bursting event, for the experimental runs 2R, 4R, 6R, and 10R, respectively.

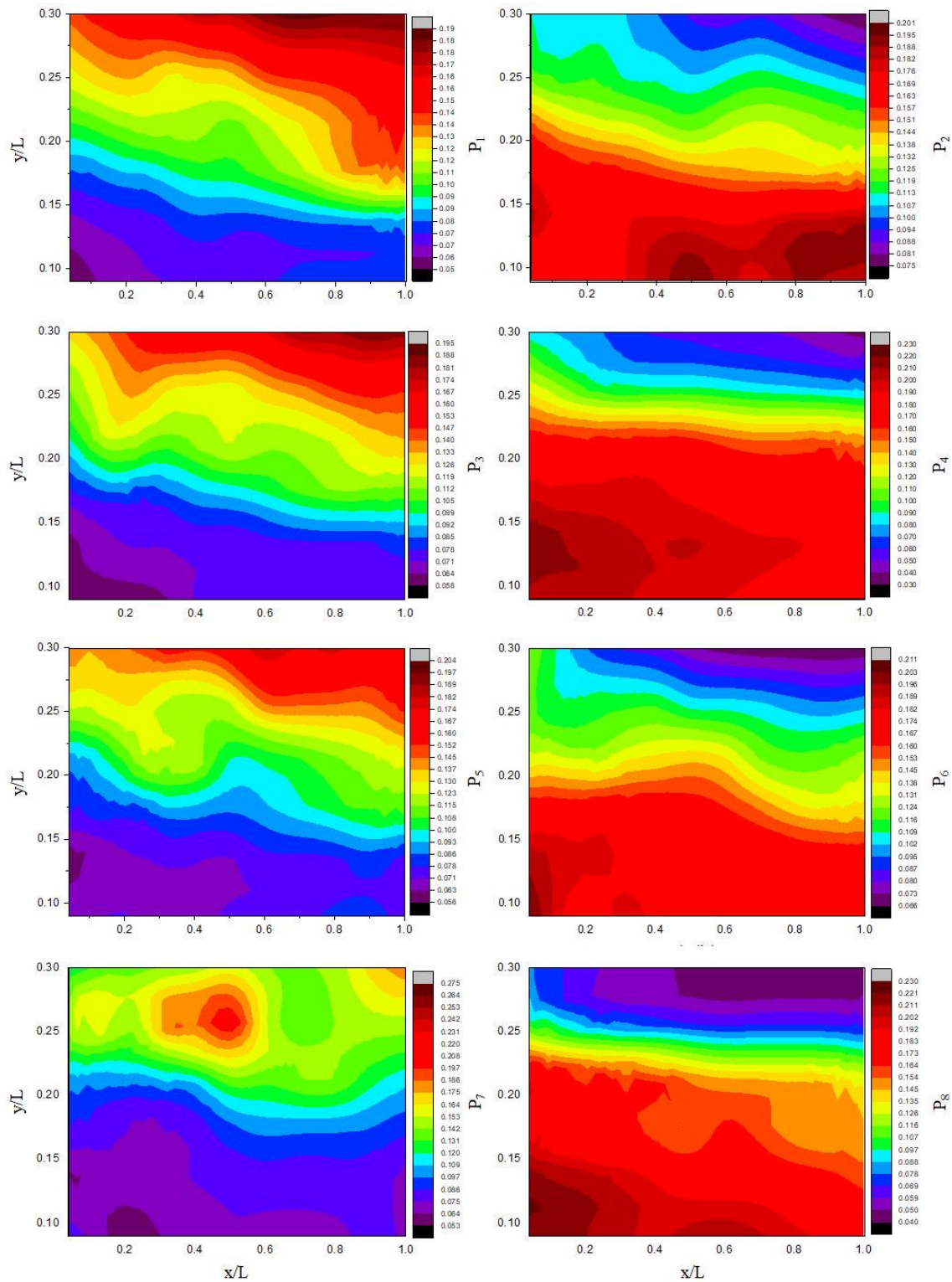


Figure 8. Contours maps of depth-averaged occurrence probability of octagonal bursting events (P_1 – P_8) for the experimental run 2R.

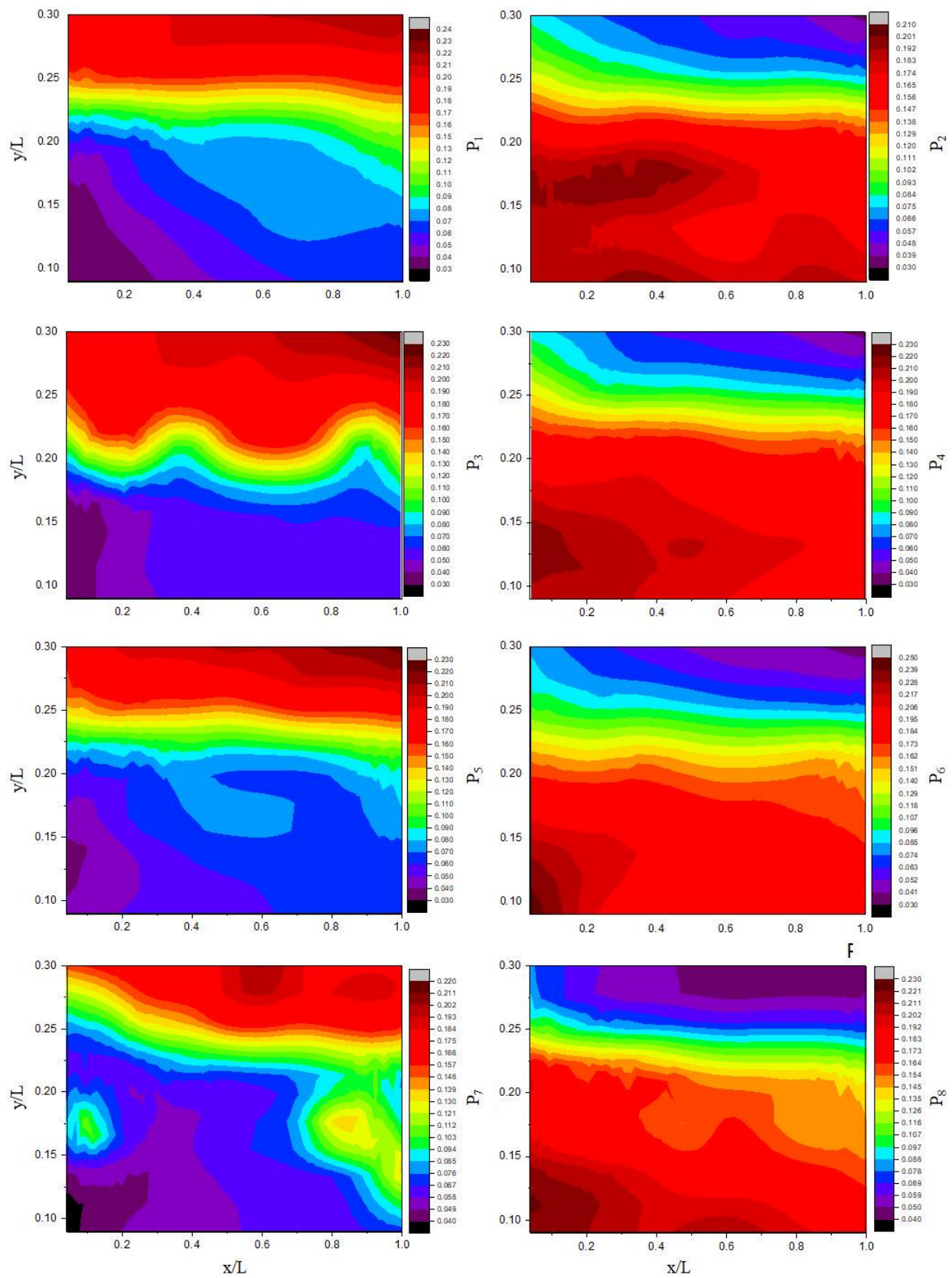


Figure 9. Contours maps of depth-averaged occurrence probability of octagonal bursting events (P₁–P₈) for the experimental run 4R.

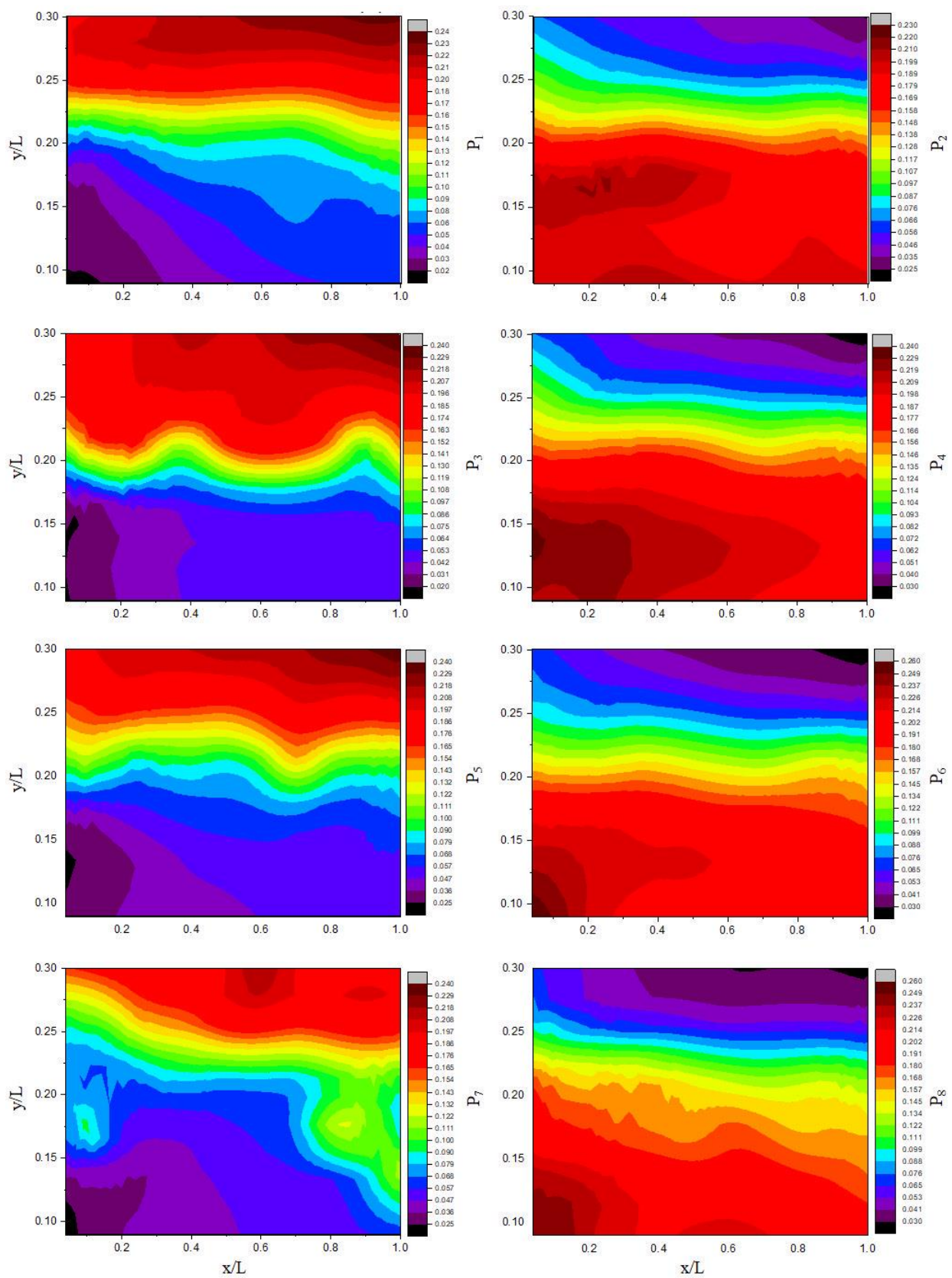


Figure 10. Contours maps of depth-averaged occurrence probability of octagonal bursting events (P_1 – P_8) for the experimental run 6R.

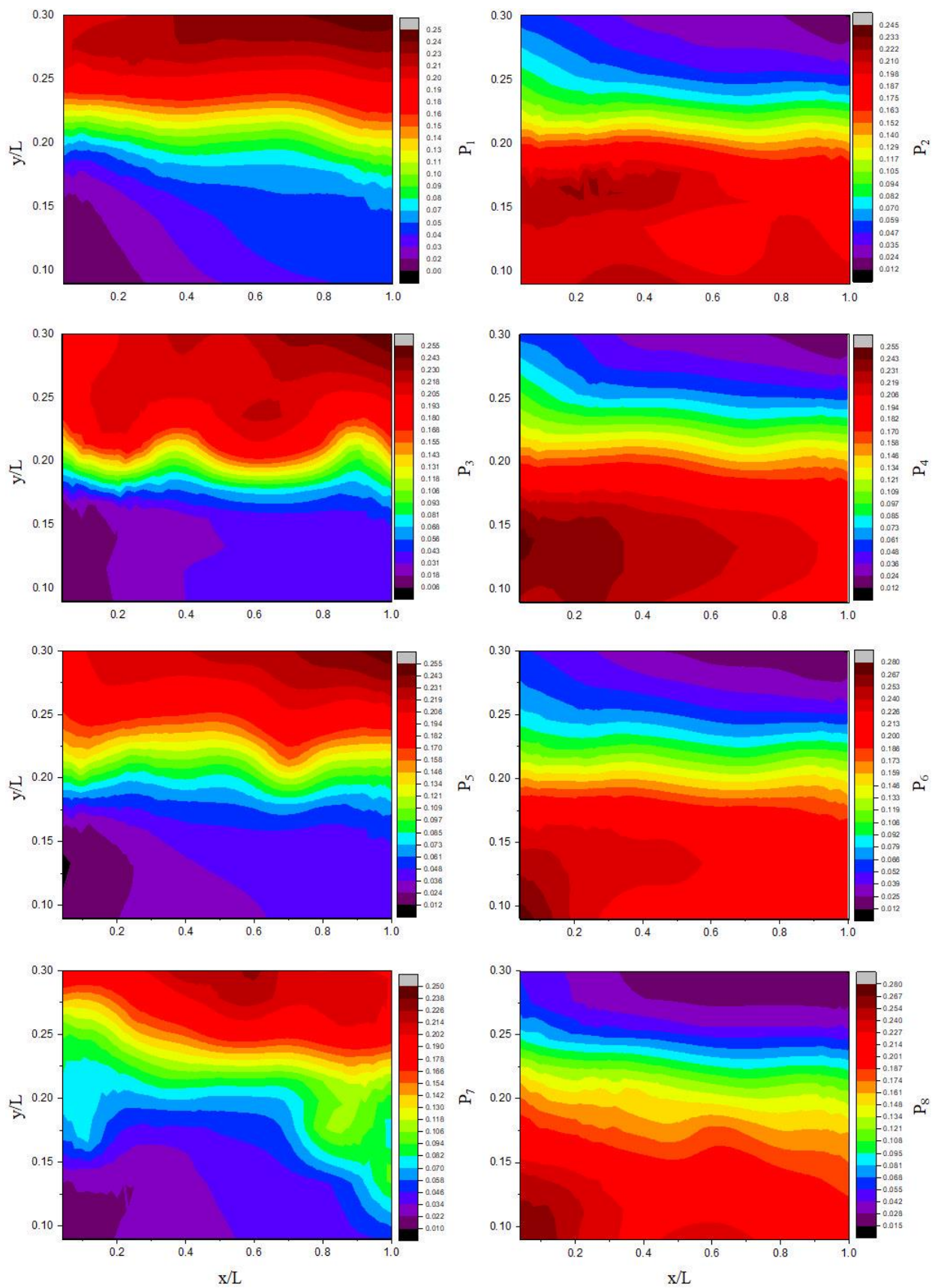


Figure 11. Contours maps of depth-averaged occurrence probability of octagonal bursting events (P₁–P₈) for the experimental run 10R.

From the comparative analysis of Figures 8–11, it was detected that the even octagonal bursting events (P_2 , P_4 , P_6 , and P_8) were dominant in the case of transverse distances $y/L \leq 0.2$, while the odd octagonal bursting events (P_1 , P_3 , P_5 , and P_7) play a crucial role for values of $y/L > 0.2$.

In addition, it was possible to observe that the peak occurrence probabilities associated with both even and odd octagonal bursting events appeared in the three-dimensional water flow region located between $x/L \leq 0.4$ and $0.6 < x/L \leq 1.0$, and between $y/L \leq 0.2$ and $y/L > 0.2$.

3.3. Analysis of Three-Dimensional Hole Size (3DHS)

Figures 12–15 display, respectively, the variations in the occurrence probabilities of the octagonal bursting events (P_1 – P_8) as a function of 3DHS at the measuring points “2”, “4”, “6”, and “10” for the experimental runs 2R, 4R, 6R, and 10R.

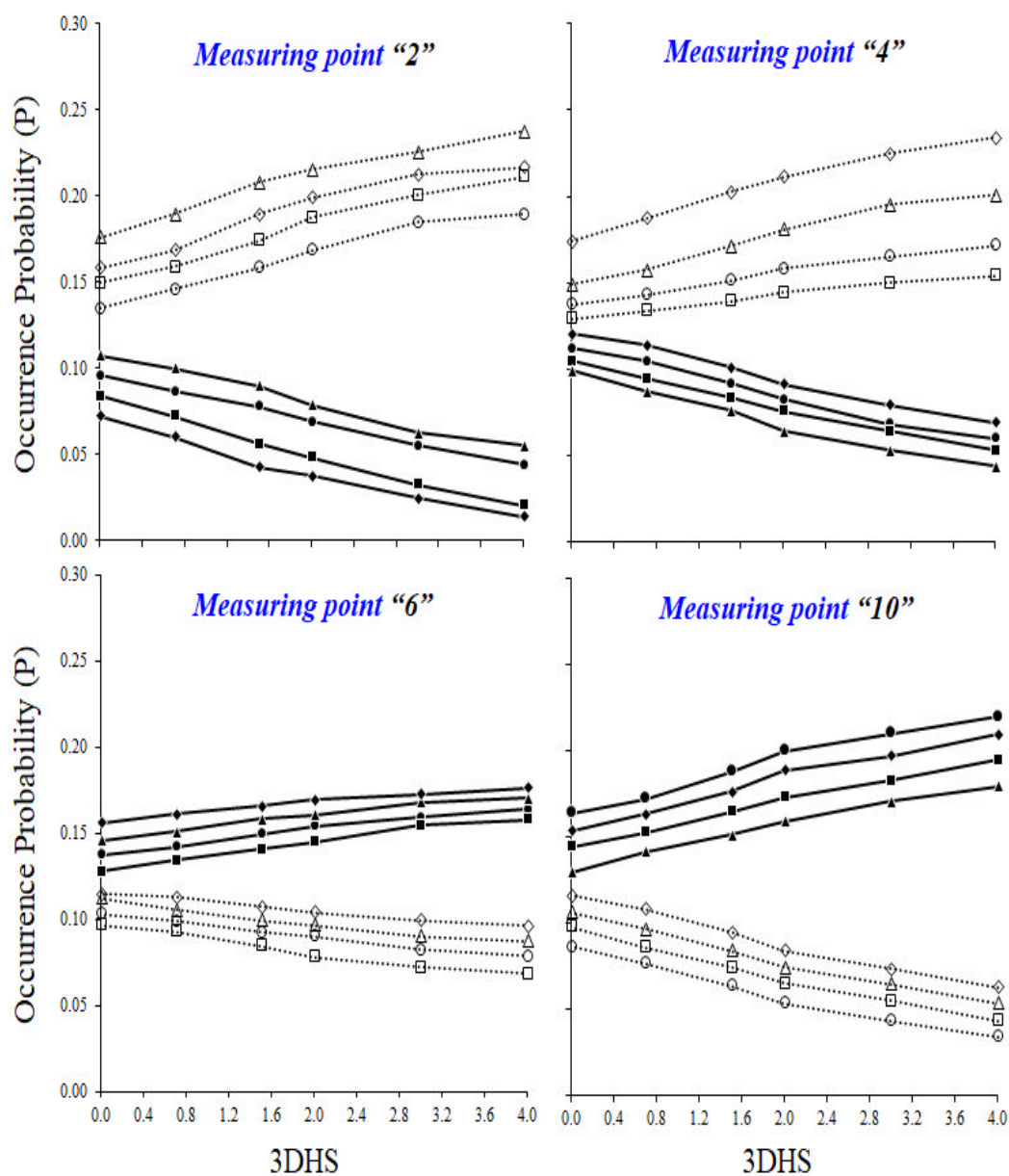


Figure 12. Depth-averaged occurrence probabilities of the octagonal bursting events with 3DHS values for the experimental run 2R: P_1 (filled circles), P_2 (unfilled circles), P_3 (filled squares), P_4 (unfilled squares), P_5 (filled triangles), P_6 (unfilled triangles), P_7 (filled diamonds), and P_8 (unfilled diamonds). Continuous lines indicate odd octagonal events, while dashed lines denote even events.

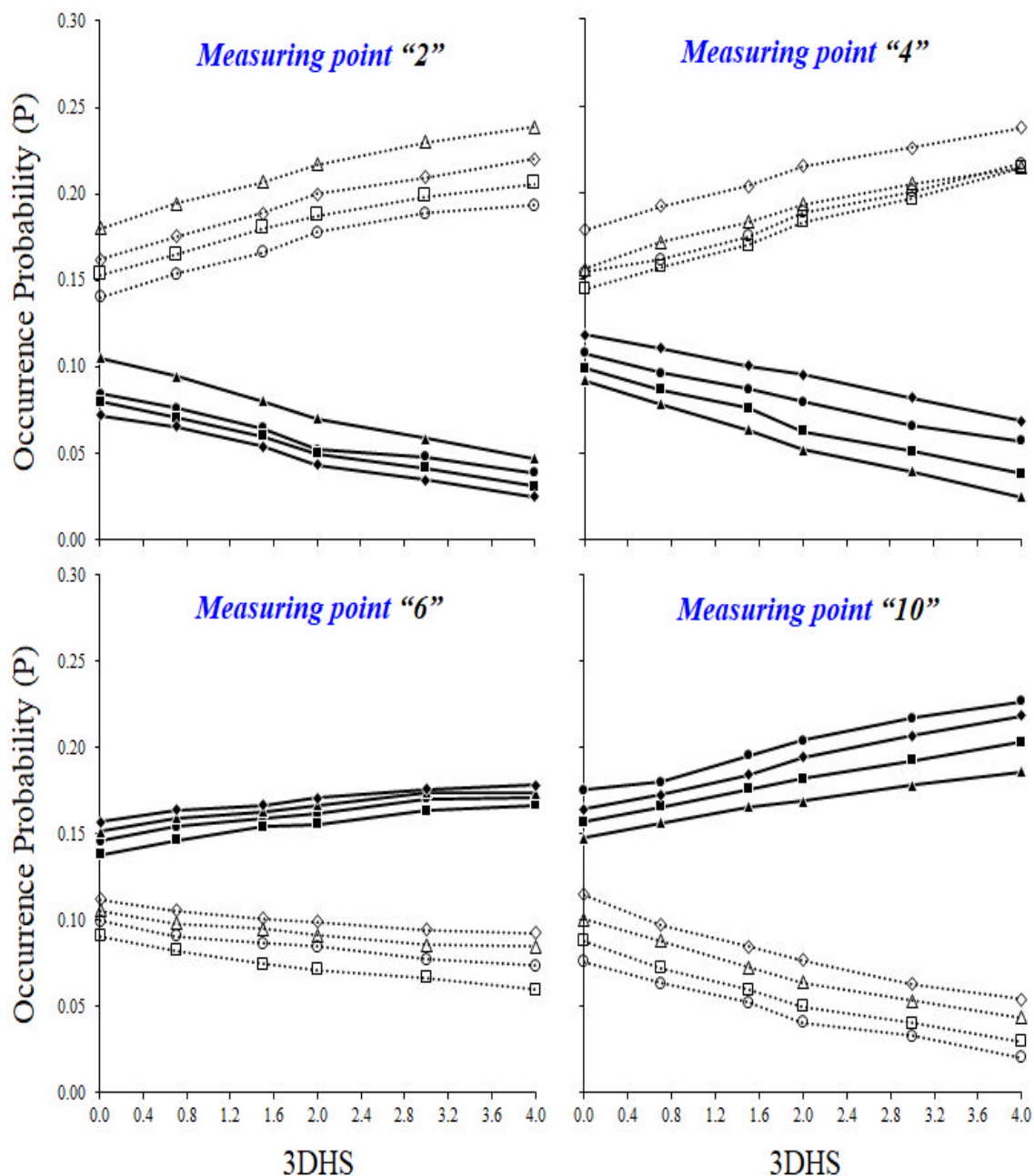


Figure 13. Depth-averaged occurrence probabilities of the octagonal bursting events with 3DHS values for the experimental run 4R: P₁ (filled circles), P₂ (unfilled circles), P₃ (filled squares), P₄ (unfilled squares), P₅ (filled triangles), P₆ (unfilled triangles), P₇ (filled diamonds), and P₈ (unfilled diamonds). Continuous lines indicate odd octagonal events, while dashed lines denote even events.

As reported in Figure 12, the depth-averaged occurrence probability corresponding to even octagonal bursting events is noticeably larger (at least two times) than that associated with odd ones at the measuring points "2" and "4", placed near the upstream end of the emerging sand bar, while it decreases with 3DHS values systematically. On the contrary, nearby the downstream end of the experimental bar, at the measuring points "6" and "10", the depth-averaged occurrence probabilities corresponding to the odd octagonal turbulence bursting events were higher than those observed in the case of even bursting events [88–94].

From the analysis of Figures 13–15, it was possible to detect that the depth-averaged occurrence probabilities associated with even octagonal bursting turbulence events grew with increasing h_b/h values at the upstream end of the examined bar, and the same

hydrodynamic pattern was recognized in the odd events close to the downstream end of the emerging sand bar [95–99].

The potential of the 3D water turbulence analysis reported in the present experimental study can be certainly increased through the support of the most advanced reinforcement and deep learning approaches, widely employed in recent ecohydraulic studies dealing with water resources management [100–103].

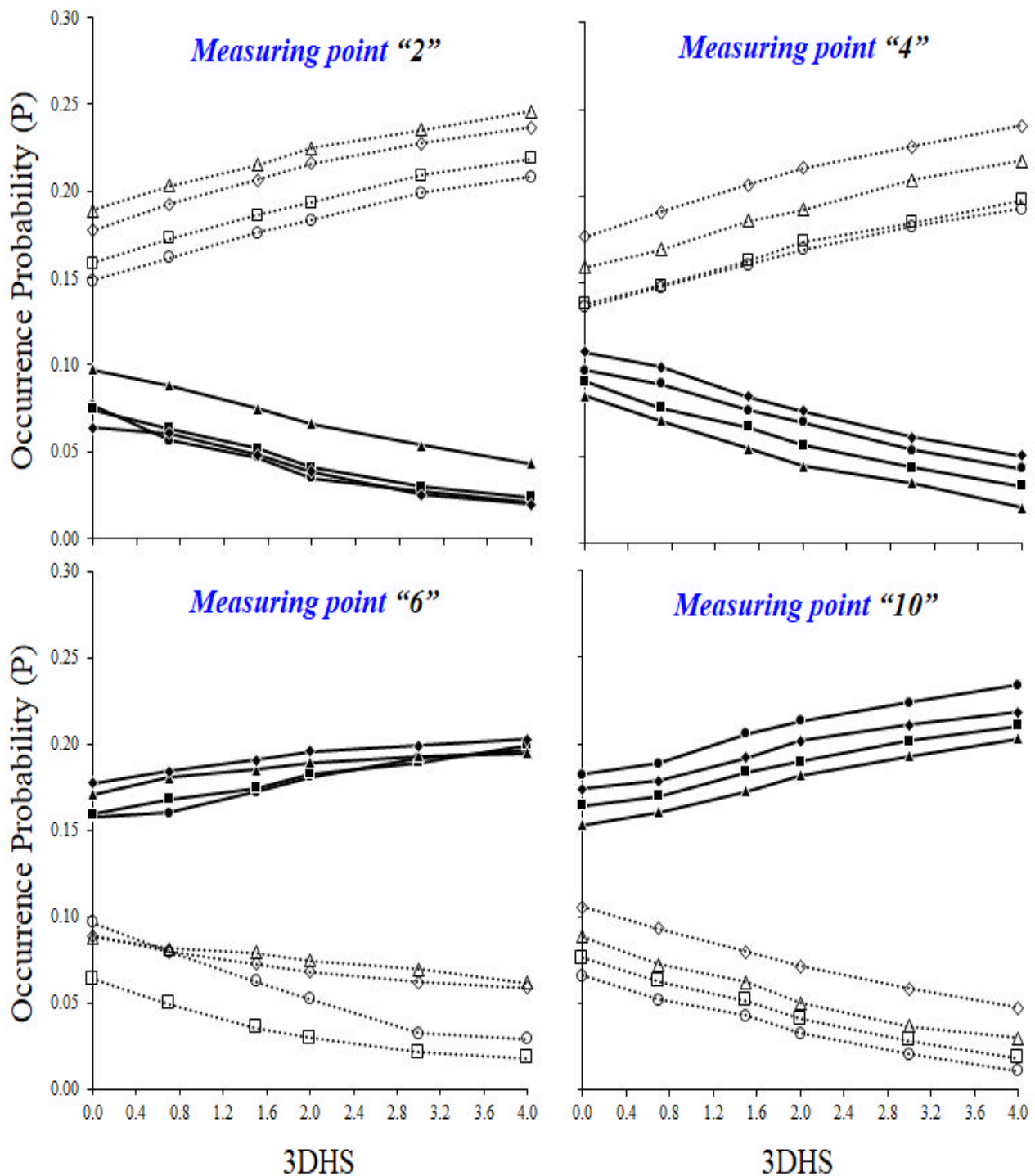


Figure 14. Depth-averaged occurrence probabilities of the octagonal bursting events with 3DHS values for the experimental run 6R: P_1 (filled circles), P_2 (unfilled circles), P_3 (filled squares), P_4 (unfilled squares), P_5 (filled triangles), P_6 (unfilled triangles), P_7 (filled diamonds), and P_8 (unfilled diamonds). Continuous lines indicate odd octagonal events, while dashed lines denote even events.

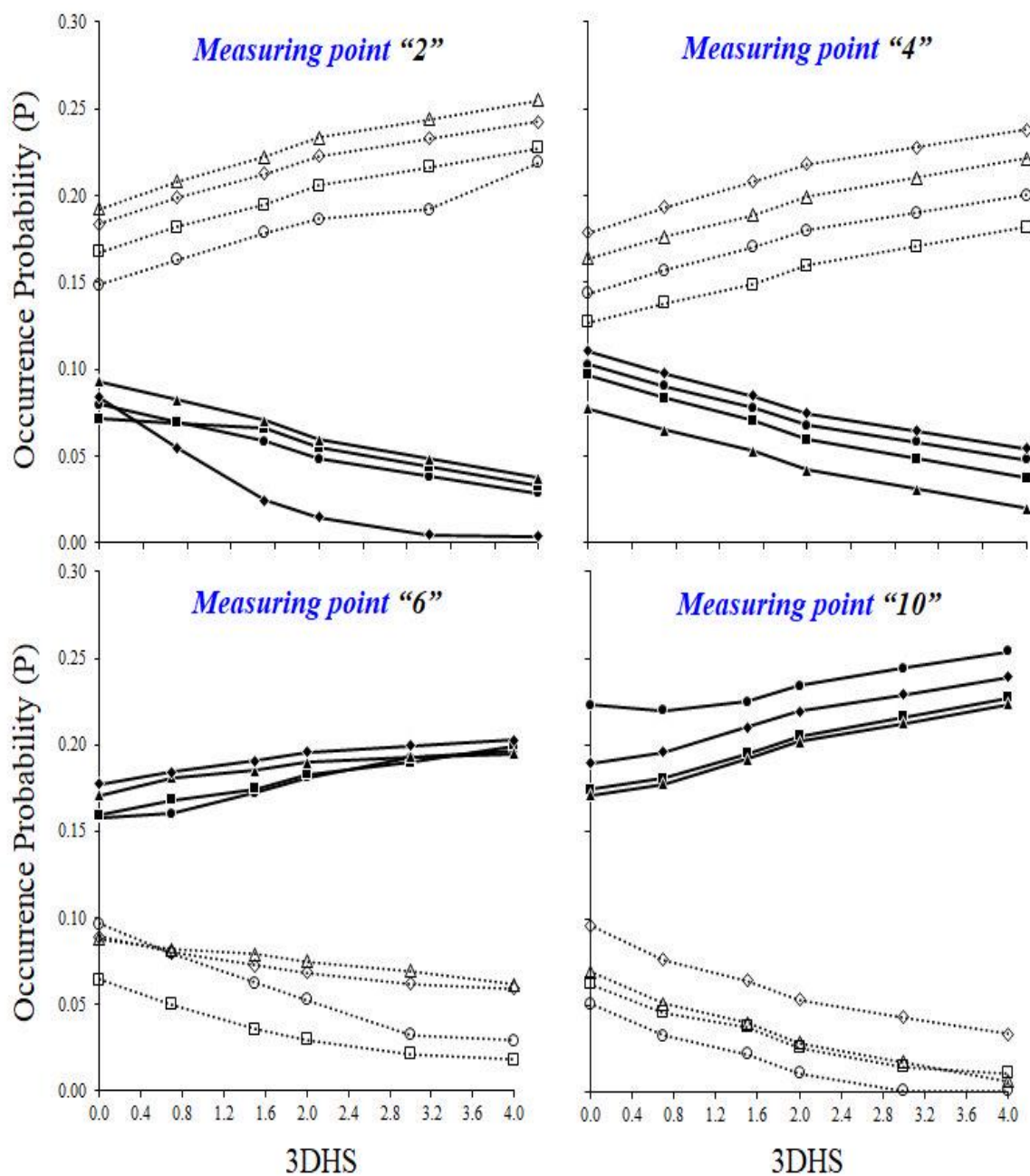


Figure 15. Depth-averaged occurrence probabilities of the octagonal bursting events with 3DHS values for the experimental run 10R: P₁ (filled circles), P₂ (unfilled circles), P₃ (filled squares), P₄ (unfilled squares), P₅ (filled triangles), P₆ (unfilled triangles), P₇ (filled diamonds), and P₈ (unfilled diamonds). Continuous lines indicate odd octagonal events, while dashed lines denote even events.

4. Conclusions

The present experimental research represents an extremely useful insight into the comprehension of the hydrodynamic interaction between local streambed elevation changes and 3D turbulent bursting events observed in the vicinity of the emerging sand bar.

An innovative threshold method based on the so-defined 3D Hole Size (3DHS) analysis was proposed here to study the 3D water flow structures observed over the examined emerging sand bar, obtained by extending the theoretical background of the well-known 2D Hole Size approach [104–107].

The experimental outcomes of the analysis performed in this work well indicate that the three-dimensional water flow fields induced by the presence of the emerging bar

produced high values of even and odd octagonal bursting events near the upstream and the downstream end of the experimental bar model, respectively. Following the 3DHS methodology, it was observed that the occurrence probability of dominant events further increases with increasing 3DHS and h_b/h values. The main goal of furnishing a useful and simple tool for both hydrodynamic and environmental researchers for the analysis of 3D turbulence over braided rivers was accomplished through the present flume-scale experimental study.

Author Contributions: Conceptualization, M.A.K., N.S., G.F.C.L., M.H., R.G., G.B. and R.S.A.; methodology, M.A.K., N.S., G.F.C.L., M.H., R.G., G.B. and R.S.A.; formal analysis, M.A.K., N.S., G.F.C.L., M.H., R.G., G.B. and R.S.A.; investigation, M.A.K., N.S., G.F.C.L., M.H., R.G., G.B. and R.S.A.; data curation, M.A.K., N.S., G.F.C.L., M.H., R.G., G.B. and R.S.A.; writing—original draft preparation, M.A.K., N.S., G.F.C.L., M.H., R.G., G.B. and R.S.A.; writing—review and editing, M.A.K., N.S., G.F.C.L., M.H., R.G., G.B. and R.S.A. All authors have read and agreed to the published version of the manuscript.

Funding: The authors would like to acknowledge the support provided by Researchers Supporting Project number (RSP-2021/310), King Saud University, Riyadh, Saudi Arabia.

Institutional Review Board Statement: Not applicable.

Informed Consent Statement: Informed consent was obtained from all subjects involved in the study.

Data Availability Statement: The data presented in this study are available on request from the corresponding author.

Conflicts of Interest: The authors declare no conflict of interest.

References

1. Wang, B.; Xu, Y.J. Sediment Trapping by Emerged Channel Bars in the Lowermost Mississippi River during a Major Flood. *Water* **2015**, *7*, 6079–6096. [\[CrossRef\]](#)
2. Wu, S.; Xu, Y.J.; Wang, B.; Cheng, H. Riverbed dune morphology of the Lowermost Mississippi River – Implications of leeside slope, flow resistance and bedload transport in a large alluvial river. *Geomorphology* **2021**, *385*, 107733. [\[CrossRef\]](#)
3. Garambois, P.-A.; Calmant, S.; Roux, H.; Paris, A.; Monnier, J.; Finaud-Guyot, P.; Samine Montazem, A.; Santos da Silva, J. Hydraulic visibility: Using satellite altimetry to parameterize a hydraulic model of an ungauged reach of a braided river. *Hydrol. Process.* **2017**, *31*, 756–767. [\[CrossRef\]](#)
4. Lama, G.F.C.; Crimaldi, M.; De Vivo, A.; Chirico, G.B.; Sarghini, F. Eco-hydrodynamic characterization of vegetated flows derived by UAV-based imagery. In Proceedings of the 2021 IEEE International Workshop on Metrology for Agriculture and Forestry (MetroAgriFor), Trento-Bolzano, Italy, 3–5 November 2021; pp. 273–278. [\[CrossRef\]](#)
5. Javernick, L.; Redolfi, M.; Bertoldi, W. Evaluation of a numerical model's ability to predict bed load transport observed in braided river experiments. *Adv. Water Resour.* **2018**, *115*, 207–218. [\[CrossRef\]](#)
6. Donadio, C.; Brescia, M.; Riccardo, A.; Angora, G.; Delli Veneri, M.; Riccio, G. A novel approach to the classification of terrestrial drainage networks based on deep learning and preliminary results on solar system bodies. *Sci. Rep.* **2021**, *11*, 5875. [\[CrossRef\]](#) [\[PubMed\]](#)
7. Gurnell, A.M.; Bertoldi, W.; Francis, R.A.; Gurnell, J.; Mardhiah, U. Understanding processes of island development on an island braided river over timescales from days to decades. *Earth Surf. Process. Landf.* **2019**, *44*, 624–640. [\[CrossRef\]](#)
8. Tauro, F. River basins on the edge of change. *Science* **2021**, *372*, 680–681. [\[CrossRef\]](#) [\[PubMed\]](#)
9. Lama, G.F.C.; Crimaldi, M.; Pasquino, V.; Padulano, R.; Chirico, G.B. Bulk Drag Predictions of Riparian *Arundo donax* Stands through UAV-acquired Multispectral Images. *Water* **2021**, *13*, 1333. [\[CrossRef\]](#)
10. Yücesan, S.; Schobesberger, J.; Sindelar, C.; Hauer, C.; Habersack, H.; Tritthart, M. Large Eddy Simulation of a sediment particle under entrainment conditions. *J. Hydraul. Res.* **2022**, *60*, 568–587. [\[CrossRef\]](#)
11. Tang, C.; Li, Y.; Acharya, K.; Du, W.; Gao, X.; Luo, L.; Yu, Z. Impact of intermittent turbulent bursts on sediment resuspension and internal nutrient release in Lake Taihu, China. *Environ. Sci. Pollut. Res.* **2019**, *26*, 16519–16528. [\[CrossRef\]](#)
12. Zordan, J.; Juez, C.; Schleiss, A.J.; Franca, M.J. Entrainment, transport and deposition of sediment by saline gravity currents. *Adv. Water Resour.* **2018**, *115*, 17–32. [\[CrossRef\]](#)
13. McSherry, R.; Chua, K.; Stoesser, T.; Mulahasan, S. Free surface flow over square bars at intermediate relative submergence. *J. Hydraul. Res.* **2018**, *56*, 825–843. [\[CrossRef\]](#)
14. Jalalabadi, R.; Stoesser, T.; Ouro, P.; Luo, Q.; Xie, Z. Free surface flow over square bars at different Reynolds numbers. *J. Hydro-environ. Res.* **2021**, *36*, 67–76. [\[CrossRef\]](#)
15. González, C.; Richter, D.H.; Bolster, D.; Bateman, S.; Calantoni, J.; Escauriaza, C. Characterization of bedload intermittency near the threshold of motion using a Lagrangian sediment transport model. *Environ. Fluid Mech.* **2017**, *17*, 111–137. [\[CrossRef\]](#)

16. Branß, T.; Núñez-González, F.; Aberle, J. Fluvial levees in compound channels: A review on formation processes and the impact of bedforms and vegetation. *Environ. Fluid Mech.* **2022**, *22*, 559–585. [\[CrossRef\]](#)
17. Hamidouche, S.; Calluau, D.; Pineau, G.; Texier, A. Study of instantaneous flow behind a single fixed ripple. *J. Hydro-environ. Res.* **2018**, *19*, 117–127. [\[CrossRef\]](#)
18. Guillén Ludeña, S.; Cheng, Z.; Constantinescu, G.; Franca, M.J. Hydrodynamics of mountain-river confluences and its relationship to sediment transport. *J. Geophys. Res. Earth Surf.* **2017**, *122*, 901–924. [\[CrossRef\]](#)
19. Peruzzi, C.; Poggi, D.; Ridolfi, L.; Manes, C. On the scaling of large-scale structures in smooth-bed turbulent open-channel flows. *J. Fluid Mech.* **2020**, *889*, A1. [\[CrossRef\]](#)
20. Cheng, Z.; Koken, M.; Constantinescu, G. Approximate methodology to account for effects of coherent structures on sediment entrainment in RANS simulations with a movable bed and applications to pier scour. *Adv. Water Resour.* **2018**, *120*, 65–82. [\[CrossRef\]](#)
21. Peruzzi, C.; Vettori, D.; Poggi, D.; Blondeaux, P.; Ridolfi, L.; Manes, C. On the influence of collinear surface waves on turbulence in smooth-bed open-channel flows. *J. Fluid Mech.* **2021**, *924*, A6. [\[CrossRef\]](#)
22. Tsai, C.W.; Huang, S.-H.; Hung, S.Y. Incorporating the memory effect of turbulence structures into suspended sediment transport modeling. *Water Resour. Res.* **2021**, *57*, e2020WR028475. [\[CrossRef\]](#)
23. Sharma, A. Velocity Distribution and the Moments of Turbulent Flow over a Sand-Gravel Mixture Bed. *Water Resour.* **2021**, *49*, 81–87. [\[CrossRef\]](#)
24. Nakagawa, H.; Nezu, I. Prediction of the contributions to the Reynolds stress from bursting events in open-channel flows. *J. Fluid Mech.* **1977**, *80*, 99. [\[CrossRef\]](#)
25. Lu, S.S.; Willmarth, W.W. Measurements of the structure of the Reynolds stress in a turbulent boundary layer. *J. Fluid Mech.* **1973**, *60*, 481–511. [\[CrossRef\]](#)
26. Gualtieri, P.; De Felice, S.; Pasquino, V.; Pulci Doria, G. Use of conventional flow resistance equations and a model for the Nikuradse roughness in vegetated flows at high submergence. *JOHH* **2018**, *66*, 107–120. [\[CrossRef\]](#)
27. Lama, G.F.C.; Errico, A.; Francalanci, S.; Solari, L.; Preti, F.; Chirico, G.B. Evaluation of Flow Resistance Models Based on Field Experiments in a Partly Vegetated Reclamation Channel. *Geosciences* **2020**, *10*, 47. [\[CrossRef\]](#)
28. Das, S.; Balachandar, R.; Barron, R. Generation and characterization of fully developed state in open channel flow. *J. Fluid Mech.* **2022**, *934*, A35. [\[CrossRef\]](#)
29. Carbonari, C.; Recking, A.; Solari, L. Morphology, Bedload, and Sorting Process Variability in Response to Lateral Confinement: Results From Physical Models of Gravel-bed Rivers. *J. Geophys. Res. Earth Surf.* **2020**, *125*, e2020JF005773. [\[CrossRef\]](#)
30. Leary, K.C.P.; Schmeeckle, M.W. The importance of splat events to the spatiotemporal structure of near-bed fluid velocity and bed load motion over bed forms: Laboratory experiments downstream of a backward facing step. *J. Geophys. Res. Earth Surf.* **2017**, *122*, 2411–2430. [\[CrossRef\]](#)
31. Schobesberger, J.; Lichtneger, P.; Hauer, C.; Habersack, H.; Sindelar, C. Three-dimensional coherent flow structures during incipient particle motion. *J. Hydraul. Eng.* **2020**, *146*, 04020027. [\[CrossRef\]](#)
32. Volino, R.J.; Simon, T.W. An Application of Octant Analysis to Turbulent and Transitional Flow Data. *ASME J. Turbomach.* **1994**, *116*, 752–758. [\[CrossRef\]](#)
33. Ninto, Y.; Garcia, M.H. Experiments on particle-turbulence interactions in the near-wall region of an open channel flow: Implications for sediment transport. *J. Fluid Mech.* **1996**, *326*, 285–319. [\[CrossRef\]](#)
34. Liu, C.; Gao, Y.; Dong, X.; Gao, Y.S.; Dong, X.R.; Wang, Y.Q.; Liu, J.M.; Zhang, Y.N.; Cai, X.S.; et al. Third generation of vortex identification methods: Omega and Liutex/Rortex based systems. *J. Hydrodyn.* **2019**, *31*, 205–223. [\[CrossRef\]](#)
35. Elsas, J.H.; Moriconi, L. Vortex identification from local properties of the vorticity field. *Phys. Fluids* **2017**, *29*, 015101. [\[CrossRef\]](#)
36. Liu, Y.; Zhong, W.; Tang, Y. On the relationships between different vortex identification methods based on local trace criterion. *Phys. Fluids* **2021**, *33*, 105116. [\[CrossRef\]](#)
37. Guan, D.; Melville, B.W.; Friedrich, H. Flow patterns and turbulence structures in a scour hole downstream of a submerged weir. *J. Hydraul. Eng.* **2014**, *140*, 68–76. [\[CrossRef\]](#)
38. Khan, M.A.; Sharma, N.; Pu, J.H.; Alfaisal, F.M.; Alam, S.; Garg, R.; Qamar, M.O. Mid-Channel Braid-Bar-Induced Turbulent Bursts: Analysis Using Octant Events Approach. *Water* **2022**, *14*, 450. [\[CrossRef\]](#)
39. Borisova, T.D.; Blagoveshchenska, N.F.; Moskvina, I.V.; Rietveld, M.T.; Kosch, M.J.; Thidé, B. Doppler shift simulation of scattered HF signals during the Tromsø HF pumping experiment on 16 February. *Ann. Geophys.* **2002**, *20*, 1479–1486. [\[CrossRef\]](#)
40. Chang, K.A.; Ariyaratne, K.; Mercier, R. Three-dimensional green water velocity on a model structure. *Exp. Fluids* **2011**, *51*, 327–345. [\[CrossRef\]](#)
41. Lama, G.F.C.; Chirico, G.B. Effects of reed beds management on the hydrodynamic behaviour of vegetated open channels. In Proceedings of the 2020 IEEE International Workshop on Metrology for Agriculture and Forestry (MetroAgriFor), Trento, Italy, 4–6 November 2020; pp. 149–154. [\[CrossRef\]](#)
42. Johnson, K.R.; Ting, F.C. Measurements of water surface profile and velocity field at a circular pier. *J. Eng. Mech.* **2003**, *129*, 502–513. [\[CrossRef\]](#)
43. Durgesh, V.; Thomson, J.; Richmond, M.C.; Polagye, B.L. Noise correction of turbulent spectra obtained from acoustic doppler velocimeters. *Flow. Meas. Instrum.* **2014**, *37*, 29–41. [\[CrossRef\]](#)

44. Lama, G.F.C.; Rillo Migliorini Giovannini, M.; Errico, A.; Mirzaei, S.; Padulano, R.; Chirico, G.B.; Preti, F. Hydraulic Efficiency of Green-Blue Flood Control Scenarios for Vegetated Rivers: 1D and 2D Unsteady Simulations. *Water* **2021**, *13*, 2620. [\[CrossRef\]](#)
45. Huang, Y.N.; Cheng, K.; Chen, S.W. On the detection of acoustic-gravity waves generated by typhoon by use of real time HF Doppler frequency shift sounding system. *Radio sci.* **1985**, *20*, 897–906. [\[CrossRef\]](#)
46. Xie, J.; Hu, P.; Pätz, T.; He, Z.; Cheng, N. Fluid-particle interaction regimes during the evolution of turbidity currents from a coupled LES/DEM model. *Adv. Water Res.* **2022**, 104171. [\[CrossRef\]](#)
47. Lama, G.F.C.; Giovannini, M.R.M.; Errico, A.; Mirzaei, S.; Chirico, G.B.; Preti, F. The impacts of Nature Based Solutions (NBS) on vegetated flows' dynamics in urban areas. In Proceedings of the 2021 IEEE International Workshop on Metrology for Agriculture and Forestry (MetroAgriFor), Trento-Bolzano, Italy, 3–5 November 2021; pp. 58–63. [\[CrossRef\]](#)
48. Calvo, L.; De Padova, D.; Mossa, M.; Rosman, P. Non-Hydrostatic Discontinuous/Continuous Galerkin Model for Wave Propagation, Breaking and Runup. *Computation* **2021**, *9*, 47. [\[CrossRef\]](#)
49. Keshavarzi, A.; Melville, B.; Ball, J. Three-dimensional analysis of coherent turbulent flow structure around a single circular bridge pier. *Environ. Fluid Mech.* **2014**, *14*, 821–847. [\[CrossRef\]](#)
50. Lee, S.O.; Abid, I.; Hong, S.H. Effect of complex shape of pier foundation exposure on time development of scour. *Environ. Fluid Mech.* **2021**, *21*, 103–127. [\[CrossRef\]](#)
51. Nikou, N.R.; Ziaei, A.N.; Ansary, H.; McDonough, J.M. Flow field investigation in a vortex settling basin using Acoustic Doppler Velocimetry and large eddy simulation. *Water Environ. J.* **2021**, *35*, 865–883. [\[CrossRef\]](#)
52. Li, D.; Yang, Z.; Guo, M. Study of Suspended Sediment Diffusion Coefficients in Submerged Vegetation Flow. *Water Resour. Res.* **2022**, *58*, e2021WR031155. [\[CrossRef\]](#)
53. Mali, M.; De Serio, F.; Dell'Anna, M.M.; Mastroianni, P.; Damiani, L.; Mossa, M. Enhancing the performance of hazard indexes in assessing hot spots of harbour areas by considering hydrodynamic parameters. *Ecol. Indic.* **2017**, *73*, 38–45. [\[CrossRef\]](#)
54. Bianco, F.; Race, M.; Papirio, S.; Esposito, G. Removal of polycyclic aromatic hydrocarbons during anaerobic biostimulation of marine sediments. *Sci. Tot. Environ.* **2020**, *709*, 136141. [\[CrossRef\]](#) [\[PubMed\]](#)
55. Thompson, J.; Sattar, A.M.A.; Gharabaghi, B.; Warner, R.C. Event-based total suspended sediment particle size distribution model. *J. Hydrol.* **2016**, *536*, 236–246. [\[CrossRef\]](#)
56. Chavan, R.; Gualtieri, P.; Kumar, B. Turbulent Flow Structures and Scour Hole Characteristics around Circular Bridge Piers over Non-Uniform Sand Bed Channels with Downward Seepage. *Water* **2019**, *11*, 1580. [\[CrossRef\]](#)
57. Bianco, F.; Monteverde, G.; Race, M.; Papirio, S.; Esposito, G. Comparing performances, costs and energy balance of ex situ remediation processes for PAH-contaminated marine sediments. *Environ. Sci. Pollut. Res.* **2020**, *27*, 19363–19374. [\[CrossRef\]](#)
58. Palermo, M.; Bombardelli, F.A.; Pagliara, S.; Kuroiwa, J. Time-dependent scour processes on granular beds at large scale. *Environ. Fluid Mech.* **2021**, *21*, 791–816. [\[CrossRef\]](#)
59. Lama, G.F.C.; Crimaldi, M. Remote Sensing of Ecohydrological, Ecohydraulic, and Ecohydrodynamic Phenomena in Vegetated Waterways: The Role of Leaf Area Index (LAI). *Biol. Life Sci. Forum* **2021**, *3*, 54. [\[CrossRef\]](#)
60. Waldschläger, K.; Brückner, M.Z.M.; Almroth, B.C.; Hackney, C.R.; Adyel, T.M.; Alimi, S.O.; Belontz, S.L.; Cowger, W.; Doyle, D.; Gray, A.; et al. Learning from natural sediments to tackle microplastics challenges: A multidisciplinary perspective. *Earth-Sci. Rev.* **2022**, *228*, 104021. [\[CrossRef\]](#)
61. Huang, A.; Liu, X.; Peng, W.; Dong, F.; Ma, B.; Li, J.; Wang, W. Spatiotemporal Characteristics, Influencing Factors and Evolution Laws of Water Exchange Capacity of Poyang Lake. *J. Hydrol.* **2022**, *609*, 127717. [\[CrossRef\]](#)
62. Qi, M.; Li, J.; Chen, Q.; Zhang, Q. Roughness effects on near-wall turbulence modelling for open-channel flows. *J. Hydraul. Res.* **2018**, *56*, 648–661. [\[CrossRef\]](#)
63. Ali, N.; Hamilton, N.; Calaf, M.; Cal, R.B. Turbulence kinetic energy budget and conditional sampling of momentum, scalar, and intermittency fluxes in thermally stratified wind farms. *J. Turbul.* **2019**, *20*, 32–63. [\[CrossRef\]](#)
64. Przyborowski, L.; Łoboda, A.M. Identification of coherent structures downstream of patches of aquatic vegetation in a natural environment. *J. Hydrol.* **2021**, *596*, 126123. [\[CrossRef\]](#)
65. Zhang, X.; Nepf, H.M. Reconfiguration of and drag on marsh plants in combined waves and current. *J. Fluids Struct.* **2022**, *110*, 103539. [\[CrossRef\]](#)
66. Park, G.I.; Wallace, J.M.; Wu, X.; Moin, P. Boundary layer turbulence in transitional and developed states. *Phys. Fluids* **2012**, *24*, 035105. [\[CrossRef\]](#)
67. Bauri, K.P.; Sarkar, A. Turbulent bursting events within equilibrium scour holes around aligned submerged cylinder. *J. Turbul.* **2020**, *21*, 53–83. [\[CrossRef\]](#)
68. Yuan, S.; Tang, H.; Li, K.; Xu, L.; Xiao, Y.; Gualtieri, C.; Rennie, C.; Melville, B. Hydrodynamics, sediment transport and morphological features at the confluence between the Yangtze River and the Poyang Lake. *Water Resour. Res.* **2021**, *57*, e2020WR028284. [\[CrossRef\]](#)
69. Yuan, S.; Zhu, Y.; Tang, H.; Xu, L.; Li, K.; Xiao, Y.; Gualtieri, C. Planform evolution and hydrodynamics near the multi-channel confluence between the Yarlung Zangbo River and the delta of the Niyang River. *Geomorphology* **2022**, *402*, 108157. [\[CrossRef\]](#)
70. Ölçmen, S.M.; Simpson, R.L.; Newby, J.W. Octant analysis based structural relations for three-dimensional turbulent boundary layers. *Phys. Fluids* **2006**, *18*, 02510. [\[CrossRef\]](#)
71. Keylock, C.J.; Lane, S.N.; Richards, K.S. Quadrant/octant sequencing and the role of coherent structures in bed load sediment entrainment. *J. Geophys. Res. Earth Surf.* **2014**, *119*, 264–286. [\[CrossRef\]](#)

72. Shi, Y.; Xia, Z.; Chen, S. A new identification method in sampled quadrant analysis for wall-bounded turbulence. *Phys. Fluids* **2016**, *28*, 061702. [\[CrossRef\]](#)
73. Wallace, J.M. Quadrant analysis in turbulence research: History and evolution. *Annu. Rev. Fluid Mech.* **2016**, *48*, 131–158. [\[CrossRef\]](#)
74. Xu, F.; Zhong, S.; Zhang, S. Experimental study on secondary flow in turbulent boundary layer over spanwise heterogeneous microgrooves. *Phys. Fluids* **2020**, *32*, 035109. [\[CrossRef\]](#)
75. Hou, J.; Babak, L.; Hokmabad, V.; Ghaemi, S. Three-dimensional measurement of turbulent flow over a riblet surface. *Exp. Therm. Fluid Sci.* **2017**, *85*, 229–239. [\[CrossRef\]](#)
76. Di Bernardino, A.; Monti, P.; Leuzzi, G.; Querzoli, G. Turbulent Schmidt Number Measurements Over Three-Dimensional Cubic Arrays. *Boundary-Layer Meteorol.* **2020**, *174*, 231–250. [\[CrossRef\]](#)
77. De Serio, F.; Mossa, M. Analysis of mean velocity and turbulence measurements with ADCPs. *Adv. Water Resour.* **2015**, *81*, 172–185. [\[CrossRef\]](#)
78. Errico, A.; Lama, G.F.C.; Francalanci, S.; Chirico, G.B.; Solari, L.; Preti, F. Flow dynamics and turbulence patterns in a drainage channel colonized by common reed (*Phragmites australis*) under different scenarios of vegetation management. *Ecol. Eng.* **2019**, *133*, 39–52. [\[CrossRef\]](#)
79. De Padova, D.; Meftah, M.B.; Mossa, M.; Sibilla, S. A multi-phase SPH simulation of hydraulic jump oscillations and local scouring processes downstream of bed sills. *Adv. Water Resour.* **2022**, *159*, 104097. [\[CrossRef\]](#)
80. Deshpande, V.; Kumar, B. Turbulent flow structures in alluvial channels with curved cross-sections under conditions of downward seepage. *Earth Surf. Process. Landf.* **2016**, *41*, 1073–1087. [\[CrossRef\]](#)
81. Agarwal, M.; Deshpande, V.; Katoshevski, D.; Kumar, B. A novel Python module for statistical analysis of turbulence (P-SAT) in geophysical flows. *Sci. Rep.* **2021**, *11*, 3998. [\[CrossRef\]](#)
82. Dey, S.; Sakar, S.; Solari, L. Near-bed turbulence characteristics at the entrainment threshold of sediment beds. *J. Hydraul. Eng.* **2011**, *137*, 945–958. [\[CrossRef\]](#)
83. Poggi, D.; Katul, G.G.; Albertson, J.D. Momentum Transfer and Turbulent Kinetic Energy Budgets within a Dense Model Canopy. *Boundary-Layer Meteorol.* **2004**, *111*, 589–614. [\[CrossRef\]](#)
84. Franca, M.J.; Lemmin, U. Eliminating velocity aliasing in acoustic Doppler velocity profiler data. *Meas. Sci. Technol.* **2006**, *17*, 313. [\[CrossRef\]](#)
85. James, C.N.; Houze, R.A., Jr. A real-time four-dimensional Doppler dealiasing scheme. *J. Atmos. Ocean. Technol.* **2001**, *18*, 1674–1683. [\[CrossRef\]](#)
86. Gong, J.D.; Wang, L.L.; Xu, Q. A three-step dealiasing method for Doppler velocity data quality control. *J. Atmos. Ocean. Technol.* **2003**, *20*, 1738–1748. [\[CrossRef\]](#)
87. Lemmin, U.; Rolland, T. Acoustic velocity profiler for laboratory and field studies. *J. Hydraul. Eng.* **1997**, *123*, 1089–1098. [\[CrossRef\]](#)
88. Rinoshika, H.; Rinoshika, A.; Wang, J.J.; Zheng, Y. 3D flow structures behind a wall-mounted short cylinder. *Ocean Eng.* **2021**, *221*, 108535. [\[CrossRef\]](#)
89. Sadeghifar, T.; Lama, G.F.C.; Sihag, P.; Bayram, A.; Kisi, O. Wave height predictions in complex sea flows through soft computing models: Case study of Persian gulf. *Ocean Eng.* **2022**, *245*, 110467. [\[CrossRef\]](#)
90. Tang, Z.; Jiang, N. The effect of a synthetic input on small-scale intermittent bursting events in near-wall turbulence. *Phys. Fluids* **2020**, *32*, 015110. [\[CrossRef\]](#)
91. Morani, M.C.; Simão, M.; Gazur, I.; Santos, R.S.; Carravetta, A.; Fecarotta, O.; Ramos, H.M. Pressure Drop and Energy Recovery with a New Centrifugal Micro-Turbine: Fundamentals and Application in a Real WDN. *Energies* **2022**, *15*, 1528. [\[CrossRef\]](#)
92. Busico, G.; Alessandrino, L.; Mastrocicco, M. Denitrification in Intrinsic and Specific Groundwater Vulnerability Assessment: A Review. *Appl. Sci.* **2021**, *11*, 10657. [\[CrossRef\]](#)
93. Guan, D.; Agarwal, P.; Chiew, Y.M. Quadrant analysis of turbulence in a rectangular cavity with large aspect ratios. *J. Hydraul. Eng.* **2018**, *144*, 04018035. [\[CrossRef\]](#)
94. Busico, G.; Colombani, N.; Fronzi, D.; Pellegrini, M.; Tazioli, A.; Mastrocicco, M. Evaluating SWAT model performance, considering different soils data input, to quantify actual and future runoff susceptibility in a highly urbanized basin. *J. Environ. Manage.* **2020**, *266*, 110625. [\[CrossRef\]](#) [\[PubMed\]](#)
95. Lama, G.F.C.; Sadeghifar, T.; Azad, M.T.; Sihag, P.; Kisi, O. On the Indirect Estimation of Wind Wave Heights over the Southern Coasts of Caspian Sea: A Comparative Analysis. *Water* **2022**, *14*, 843. [\[CrossRef\]](#)
96. Ramos, H.M.; Morani, M.C.; Carravetta, A.; Fecarotta, O.; Adeyeye, K.; López-Jiménez, P.A.; Pérez-Sánchez, M. New Challenges towards Smart Systems' Efficiency by Digital Twin in Water Distribution Networks. *Water* **2022**, *14*, 1304. [\[CrossRef\]](#)
97. Peng, W.; Yuan, Z.; Wang, J. Attention-enhanced neural network models for turbulence simulation. *Phys. Fluids* **2022**, *34*, 025111. [\[CrossRef\]](#)
98. Khan, A.M.; Sharma, N.; Pandey, M.; Qamar, O. Turbulent characteristics of flow in the vicinity of mid-channel braid bar. *Can. J. Civ. Eng.* **2021**, *48*, 879–887. [\[CrossRef\]](#)

99. Lama, G.F.C.; Errico, A.; Francalanci, S.; Solari, L.; Preti, F.; Chirico, G.B. Comparative analysis of modeled and measured vegetative Chézy's flow resistance coefficients in a drainage channel vegetated by dormant riparian reed. In Proceedings of the International IEEE Workshop on Metrology for Agriculture and Forestry, Portici, Italy, 4–6 November 2020; pp. 180–184. [\[CrossRef\]](#)
100. Yunping, Y.; Jinhai, Z.; Mingjin, Z.; Lingling, Z.; Yude, Z.; Jianjun, W.; Weiyang, Z. Sandy riverbed shoal under anthropogenic activities: The sandy reach of the Yangtze River, China. *J. Hydrol.* **2021**, *603*, 126861. [\[CrossRef\]](#)
101. Khan, M.A.; Sharma, N.; Singhal, G.D. Experimental study on bursting events around a bar in physical model of a braided channel. *ISH J. Hydraul. Eng.* **2017**, *23*, 63–70. [\[CrossRef\]](#)
102. Manna, M.; Vacca, A.; Verzicco, R. Reverse transition of a turbulent spiral Poiseuille flow at $Ta=1500$. *J. Fluid Mech.* **2022**, *941*, A6. [\[CrossRef\]](#)
103. Yunping, Y.; Jinhai, Z.; Huaqing, Z.; Yuanfang, C.; Yude, Z.; Chenyang, W. Impact of the Three Gorges Dam on riverbed scour and siltation of the middle reaches of the Yangtze River. *Earth Surf. Process. Landf.* **2022**, *209*, 1514–1531. [\[CrossRef\]](#)
104. Khan, M.A.; Sharma, N.; Garg, R.; Biswas, T. Contribution of quadrant bursting events to the turbulent flow structure at region close to the mid-channel bar. *ISH J. Hydraul. Eng.* **2021**, 1–10. [\[CrossRef\]](#)
105. Hasan, M.S.U.; Rai, A.K.; Ahmad, Z.; Alfaisal, F.M.; Khan, M.A.; Alam, S.; Sahana, M. Hydrometeorological consequences on the water balance in the ganga river system under changing climatic conditions using land surface model. *J. King Saud Univ. Sci.* **2022**, *34*, 102065. [\[CrossRef\]](#)
106. Khan, M.D.; Sharma, N. Analysis of turbulent flow characteristics around bar using the conditional bursting technique for varying discharge conditions. *KSCE J. Civ. Eng.* **2018**, *22*, 2315–2324. [\[CrossRef\]](#)
107. Castro-Orgaz, O.; Cantero-Chinchilla, F.N.; Hager, W.H. High-order shallow water expansions in free surface flows: Application to steady overflow processes. *Ocean Eng.* **2022**, *250*, 110717. [\[CrossRef\]](#)